

# CHEMISTRY

---

## AN ASIAN JOURNAL

www.chemasianj.org

### Accepted Article

**Title:** Dual template pore engineering of whey powder derived carbon as an efficient oxygen reduction reaction electrocatalyst for primary zinc-air battery

**Authors:** Shunyao Yan, Zixun Yu, Chang Liu, Ziwen Yuan, Chaojun Wang, Junsheng Chen, Li Wei, and Yuan Chen

This manuscript has been accepted after peer review and appears as an Accepted Article online prior to editing, proofing, and formal publication of the final Version of Record (VoR). This work is currently citable by using the Digital Object Identifier (DOI) given below. The VoR will be published online in Early View as soon as possible and may be different to this Accepted Article as a result of editing. Readers should obtain the VoR from the journal website shown below when it is published to ensure accuracy of information. The authors are responsible for the content of this Accepted Article.

**To be cited as:** *Chem. Asian J.* 10.1002/asia.202000399

**Link to VoR:** <https://doi.org/10.1002/asia.202000399>

A Journal of



A sister journal of *Angewandte Chemie*  
and *Chemistry – A European Journal*

---

WILEY-VCH

**Dual template pore engineering of whey powder derived carbon as an efficient oxygen  
reduction reaction electrocatalyst for primary zinc-air battery**

Shun Yao Yan<sup>†</sup>, Zixun Yu<sup>†</sup>, Chang Liu, Ziwen Yuan, Chaojun Wang, Junsheng Chen, Li Wei\* and  
Yuan Chen\*

School of Chemical and Biomolecular Engineering, The University of Sydney, New South Wales,  
Australia, 2006

Author email: l.wei@sydney.edu.au (L.Weil) and yuan.chen@sydney.edu.au (Y. Chen)

<sup>†</sup> These authors contribute equally

## Abstract

Cost-effective and high-performance electrocatalysts for oxygen reduction reactions are needed for many energy storage and conversion devices. Here, we demonstrate that whey powder, a major by-product in the dairy industry, can be used as a sustainable precursor to produce heteroatom doped carbon electrocatalysts for ORR. Rich N and S compounds in whey powders can generate abundant catalytic active sites. However, these sites are not easily accessible by reactants of ORR. A dual-template method was used to create a hierarchical and interconnected porous structure with micropores created by  $\text{ZnCl}_2$  and large mesopores generated by fumed  $\text{SiO}_2$  particles. At the optimum mass ratio of whey powder:  $\text{ZnCl}_2$ :  $\text{SiO}_2$  at 1:3:0.8, the resulting carbon material has a large specific surface area close to  $2000 \text{ m}^2 \text{ g}^{-1}$ , containing 4.6 at.% of N with 39.7% as pyridinic N. This carbon material shows superior electrocatalytic activity for ORR, with an electron transfer number of 3.88 and a large kinetic limiting current density of  $45.40 \text{ mA cm}^{-2}$ . They were employed as ORR catalysts to assemble primary zinc-air batteries, which deliver a power density of  $84.1 \text{ mW cm}^{-2}$  and a specific capacity of  $779.5 \text{ mAh g}^{-1}$ , outperforming batteries constructed using a commercial Pt/C catalyst. Our findings open new opportunities to use an abundant biomaterial, whey powder, to create high-value-added carbon electrocatalysts for emerging energy applications.

**Keywords:** whey powder; porous carbon; electrocatalyst; oxygen reduction reaction; zinc-air battery

## Introduction

Oxygen reduction reaction (ORR) is an essential reaction in renewable energy storage and conversion devices, such as metal-air batteries and fuel cells.<sup>[1]</sup> ORR has sluggish kinetics, which is often a performance-limiting factor for these devices.<sup>[2]</sup> Platinum (Pt)-based noble metal electrocatalysts have the best catalytic activity for ORR. However, their applications are limited by their high cost and poor stability. It is desirable to have more cost-effective and high-performance ORR electrocatalysts.<sup>[3]</sup> Heteroatom doped carbon materials is a potential alternative.<sup>[3a, 4]</sup> The dopant atoms, for example, nitrogen (N), oxygen (O), boron (B), phosphorus (P), and sulfur (S), can alter electronic structures of their neighboring carbon (C) atoms and make these C atoms active catalytic sites for ORR.<sup>[5]</sup> In general, ORR carbon electrocatalysts should contain abundant heteroatom dopants to create high-density active catalytic sites and have a large specific surface area (SSA) for accommodating these sites.<sup>[6]</sup> Further, a hierarchical pore structure with interconnected micropores and mesopores is desirable because micropores and small size mesopores (<5 nm) can provide a large SSA and large-size mesopores (>5 nm) can facilitate the mass transfer.<sup>[7]</sup> It is essential to have an optimum balance between pores in different sizes.<sup>[8]</sup>

Carbon nanomaterials, such as graphene and CNTs, have been used as precursors to produce ORR carbon electrocatalysts. However, carbon nanomaterials are usually costly, and their synthesis often produces environmentally harmful by-products and wastes.<sup>[9]</sup> Because some biomass materials are at low cost, sustainable, and enriched with N, S, and P, using them as precursors to synthesize ORR carbon electrocatalysts has drawn lots of interest.<sup>[9-10]</sup> One of such biomass materials is whey powders, which is a major by-product in the dairy industry with a global production capacity of over 1.8 million tons per annum.<sup>[11]</sup> Whey powders contain roughly 80 wt.% protein, 10 wt.% carbohydrate, 5 wt.% fat, and 1 wt.% minerals. They are much cheaper (US\$0.01 per gram) than commercial electrocatalysts; for example, Pt catalysts supported on carbon substrates (Pt/C) are ~US\$100 per gram. Most of the whey powders are currently discharged directly to farmlands, and only a small portion is further

processed as a food-grade ingredient in infant formula or animal feeds.<sup>[12]</sup> Carbon materials can be synthesized by direct carbonization of whey powders. However, such carbon materials have a small SSA without pores. Potential active ORR catalytic sites created by abundant N, S, and P compounds in whey powder derived carbon materials are not accessible to electrolyte ions and reaction intermediates. To the best of our knowledge, no previous studies have demonstrated high-performance ORR electrocatalysts using whey powder derived carbon materials.

Herein, we report a high-performance ORR carbon electrocatalyst by using whey powders as the precursor. A dual template pore engineering method using both  $\text{ZnCl}_2$  and fumed silica  $\text{SiO}_2$  as templates enabled us to tune hierarchical pore structures of the carbon electrocatalysts. The mass ratio between the two types of pore-forming templates was systematically optimized. Detailed material characterization shows that at an optimal mass ratio of  $m_{\text{WP}} : m_{\text{ZnCl}_2} : m_{\text{SiO}_2}$ , the carbon electrocatalyst exhibits a large SSA and a hierarchical pore structure, and it has excellent catalytic performance for ORR, which can compete with commercial Pt electrocatalysts. The optimized carbon electrocatalyst was used to assemble primary zinc-air batteries (ZABs), which deliver excellent energy storage characteristics, outperforming ZABs assembled using a commercial Pt electrocatalyst.

## Results and Discussion

Figure 1a illustrates the dual template pore engineering method used to create hierarchical pores in whey powder-derived carbon materials. The details of the synthesis method were described in the Experimental Section. We chose  $\text{ZnCl}_2$  and fumed  $\text{SiO}_2$  particles (~10 nm in size, see Figure S1 in the Supporting Information (SI)) as templates because  $\text{ZnCl}_2$  is a commonly used template to create micropores in carbon materials.<sup>[13]</sup> During the carbonization,  $\text{Zn}^{2+}$  ions are reduced to Zn metal, which evaporates and leaves behind abundant micropores and small mesopores. Meanwhile,  $\text{SiO}_2$  particles can serve as hard templates to create voids similar to their size.<sup>[14]</sup> Further, amorphous fumed  $\text{SiO}_2$  particles can be easily washed away by 3 M KOH solution without using the more toxic HF. We

systematically varied the mass loadings of the two templates, and the resulting carbon materials were denoted as WC- $x$ - $y$ , where  $x$  or  $y$  is the mass ratio between  $\text{ZnCl}_2$  or  $\text{SiO}_2$  and whey powders, respectively. In a group of samples, we fixed the mass loading of  $\text{ZnCl}_2$  ( $x$  value) at 3 based on our previous study.<sup>[8d]</sup> The mass loading of  $\text{SiO}_2$  ( $y$ ) was also systematically varied from 0, 0.2, 0.4, 0.8, and 1.2. Alternatively, several samples without adding  $\text{ZnCl}_2$  were also prepared. Our synthesis method is highly scalable, and as a demonstration, we synthesized one batch of carbon materials in 100 g. Figure 1b shows a photo of the synthesized carbon materials.

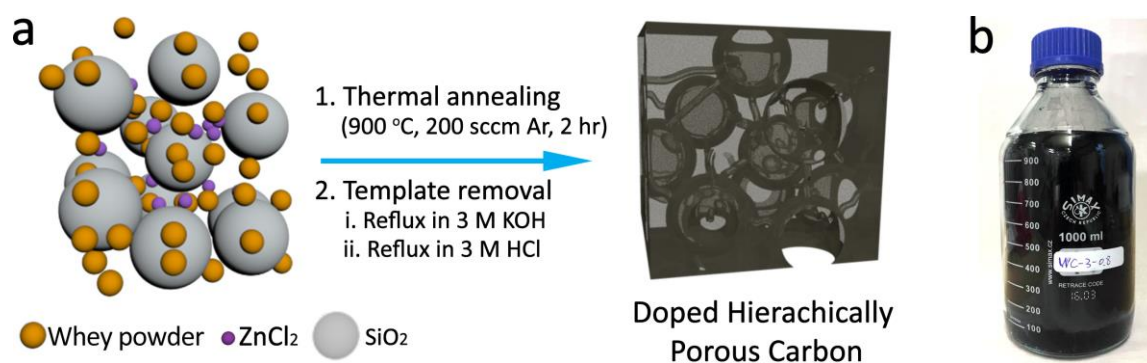


**Figure 1.** (a) Schematic illustration of the synthesis of carbon materials by the dual template method from whey powders. (b) A photo of a large batch of whey powder derived carbon materials.

We first examined the morphology of different carbon materials by scanning electron microscope (SEM). Figure 2a shows that WC-3-0.8 has a rough surface with many dents and pores. In comparison, WC-0-0.8 (Figure 2b) prepared by using  $\text{SiO}_2$  as the sole template has a similar morphology, suggesting that the observed dents/pores originate from  $\text{SiO}_2$  particles. Further, Figure S2 in SI shows SEM images of WC-3-0.2, WC-3-0.4, and WC-3-1.2. They all have rough surfaces with dents/pores. In contrast, Figure 2c shows that WC-3-0 prepared by using only the  $\text{ZnCl}_2$  template has a much smoother surface with smaller pores. When no templates were used, Figure 2d shows that WC-0-0 has a flat surface. In summary, the SEM images indicate that the morphology of carbon materials

carbonized from whey powders can be changed significantly by using different pore formation templates.

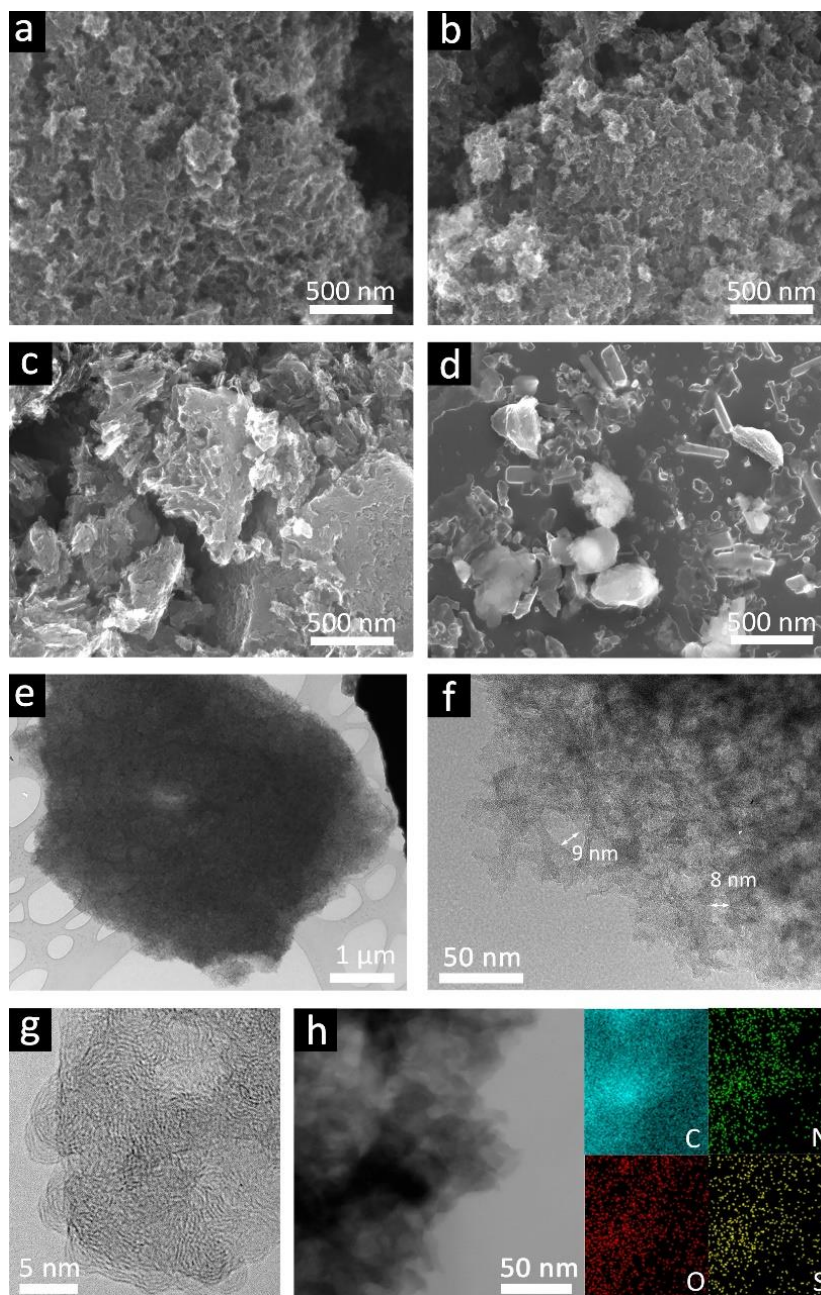


**Figure 2.** Microscopic analysis of carbon materials derived from whey powders using the dual template pore engineering method. SEM images of (a) WC-3-0.8 (dual templates), (b) WC-0-0.8 (sole SiO<sub>2</sub> template), (c) WC-3-0 (sole ZnCl<sub>2</sub> template), and (d) WC-0-0 (non-template). The scale bar is 500 nm. (e-g) TEM images at different magnifications and (h) a STEM image and the corresponding EDX elemental mappings of WC-3-0.8.

**Table 1.** Physiochemical properties of carbon materials synthesized in this study.

No	WC- <i>x-y-T</i> , <sup>[a]</sup>	N, at.% <sup>[b]</sup>	S, at.% <sup>[b]</sup>	O, at.% <sup>[b]</sup>	SSA, m <sup>2</sup> g <sup>-1</sup>	Pore volume, cm <sup>3</sup> g <sup>-1</sup>	D/G ratio
1	WC-3-0.2	4.7	1.1	9.0	896.9	0.322	1.04
2	WC-3-0.4	4.3	1.2	9.6	1232.4	0.458	1.06
3	WC-3-0.8-900	4.6	1.0	8.9	1944.7	0.635	1.10
4	WC-3-1.2	4.2	1.0	9.7	1475.7	0.497	1.05
5	WC-3-0	5.0	1.1	8.1	676.6	0.047	1.03
6	WC-0-0.8	5.3	0.9	10.0	251.4	0.147	1.00
7	WC-0-0	5.2	1.1	9.2	76.5	0.0022	1.01
8	WC-3-0.8-700	9.7	2.2	15.9	1359.6	0.412	1.18
9	WC-3-0.8-1100	1.9	0.5	7.2	1895.1	0.621	1.06

[a] Except for the samples 8 and 9, all others were carbonized at 900 °C.

[b] Determined by SEM-EDX.

Next, we measured elemental compositions of the carbon materials by energy-dispersive X-ray spectroscopy (EDX), as shown in Figure S3 in SI. As a representative example, Figure 2h shows that C, N, S, and O are the main composing elements in WC-3-0.8. The abundances of N, S, and O of all carbon materials determined by EDX are listed in Table 1, showing that the abundances of N and S are similar in all samples carbonized at 900 °C. This suggests that although the two templates can affect the surface morphology substantially, they do not influence the elemental composition strongly. It should be noted that most of Zn added evaporated during the thermal annealing, and the remnant Zn was further removed by washing in 3 M HCl for 3 h. EDX measurement showed no-detectable Zn. We further utilized the inductively coupled plasma atomic emission spectroscopy to analyze WC-3-0.8, and no Zn was found.

Further, a transmission electron microscope (TEM) was utilized to investigate the pore structures of the carbon materials. Under the lower magnification, Figure 2e shows that WC-3-0.8 has a porous structure. Under the higher magnification, Figure 2f reveals many mesopores of 8–10 nm in diameter, which are created by SiO<sub>2</sub> particles. Well-resolved lattice fringes with a *d*-spacing of ~0.35 nm can be observed in Figure 2g, indicating a high level of graphitization in carbon materials, which is beneficial for providing a high electrical conductivity. Figure 2h shows that EDX mappings obtained under the

scanning TEM mode (STEM) are consistent with the uniform elemental distribution found in SEM images (Figure S3 in SI).

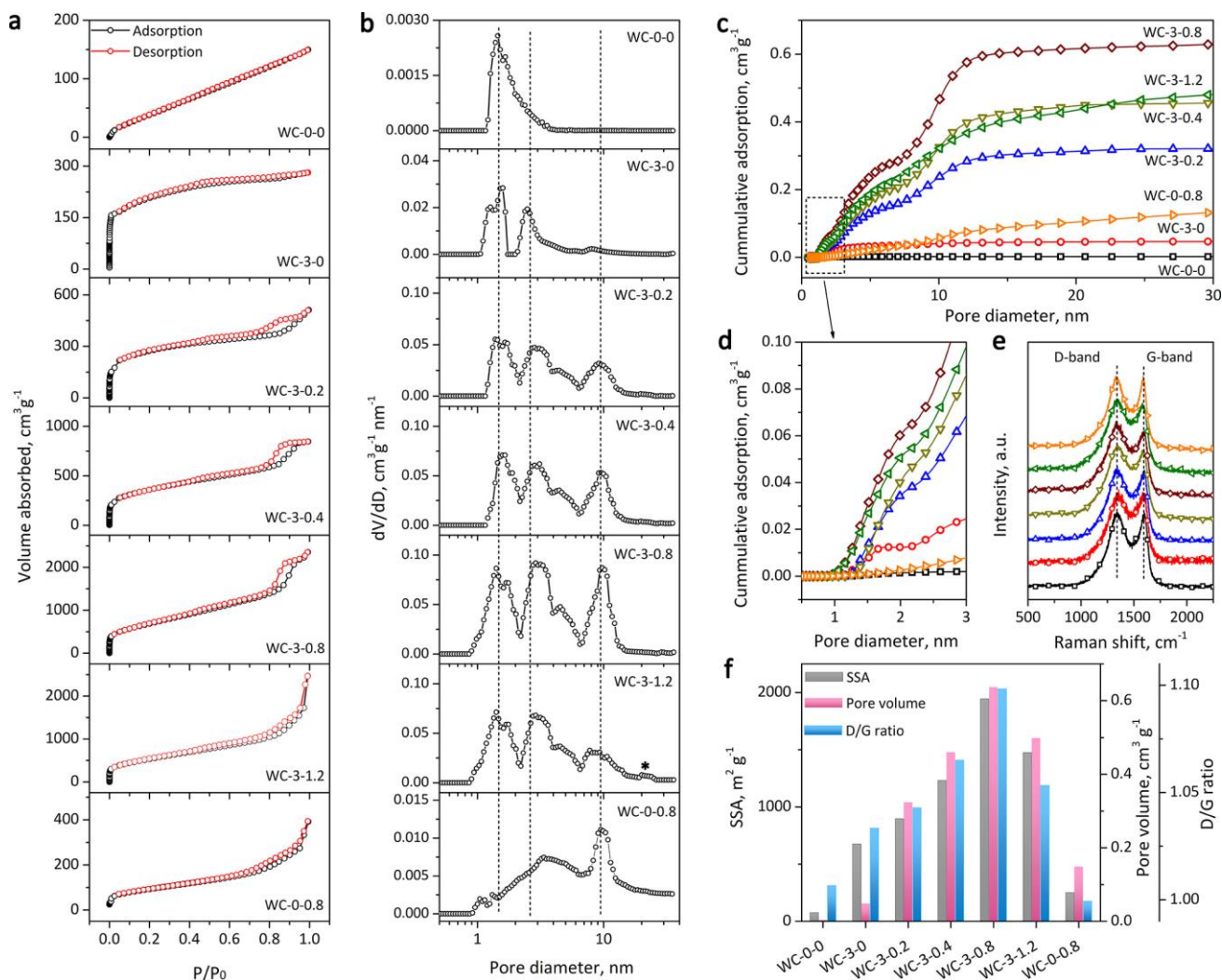


**Figure 3.** (a) N<sub>2</sub> physisorption isotherms, (b) the corresponding pore size distribution, (c) cumulative adsorption volumes, (d) magnified micropore regions of (c), and (e) Raman spectra of whey powder derived carbon materials. (f) Comparison of three physicochemical structural properties of the carbon materials: SSA, pore-volume, and Raman D/G ratio.

Nitrogen physisorption was used to study the pore structure of the carbon materials. The isotherms are shown in **Figure 3a**. Their specific surface areas are calculated by the Brunauer–Emmett–Teller (BET) method and listed in Table 1. Their pore size distributions were determined by the non-local

density functional theory (NL-DFT) model and plotted in Figure 3b for comparison. We first compared the effectiveness of  $\text{ZnCl}_2$  and  $\text{SiO}_2$  templates in creating pores. Without using any templates, WC-0-0 has an SSA of  $76.5 \text{ m}^2 \text{ g}^{-1}$  and a negligible pore volume of  $0.0022 \text{ cm}^3 \text{ g}^{-1}$ . When  $\text{ZnCl}_2$  was used, the line shape of the isotherm of WC-3-0 exhibits a combination of Type I and Type IV in the low pressure ( $P/P_0 < 0.05$ ) and high pressure ( $P/P_0 \sim 0.8$ ) regions, respectively, indicating the co-existence of both micropores and mesopores.<sup>[15]</sup> The pore-size distribution displayed in Figure 3b confirms abundant micropores with a diameter of  $\sim 1.5 \text{ nm}$  and mesopores of  $2.8 \text{ nm}$ . The SSA of WC-3-0 increases nearly 10 times to  $676.6 \text{ m}^2 \text{ g}^{-1}$  in comparison to that of WC-0-0.  $\text{SiO}_2$  particles generate pores like their size in WC-0-3 with large mesopores ( $\sim 10 \text{ nm}$ ). These large mesopores increase the pore volume to  $0.147 \text{ cm}^3 \text{ g}^{-1}$  (Figure 3c); however, they contribute less to the SSA. WC-0-3 has an SSA of  $251.4 \text{ m}^2 \text{ g}^{-1}$ .

The dual template method provides an efficient tool for engineering the pore structure and SSA of whey powder derived carbon materials. As shown in Figure 3c, both the SSA and pore volume increase with the increase of the mass loadings of  $\text{SiO}_2$ . At an optimal mass loading of  $\text{SiO}_2$  particles to whey powder at 0.8, WC-3-0.8 has the maximum SSA of  $1944.7 \text{ m}^2 \text{ g}^{-1}$  and the largest pore volume of  $0.635 \text{ cm}^3 \text{ g}^{-1}$  among all the carbon materials. There is an increasing trend of the S-curve slopes in the micropore/small-mesopore region (1–3 nm), as displayed in Figure 3d. This suggests that large mesopores created by  $\text{SiO}_2$  particles may have formed interconnected pores, which expose buried micropores and small mesopores formed by  $\text{ZnCl}_2$ . However, further increasing the mass loadings of  $\text{SiO}_2$  deteriorates the pore structure of WC-3-1.2 due to the aggregation of  $\text{SiO}_2$  particles. WC-3-1.2 exhibits a reduced SSA of  $1475.7 \text{ m}^2 \text{ g}^{-1}$  and a smaller pore volume of  $0.497 \text{ cm}^3 \text{ g}^{-1}$  compared to WC-3-0.8. The pore size distribution curve of WC-3-1.2 exhibits a broadened peak of large mesopores and a new peak at around  $20 \text{ nm}$  (marked by \* in Figure 3b). Its S-curve in Figure 3c also exhibits an extended increasing trend, indicating the formation of larger pores.

We further collected Raman spectra of the carbon materials to study the impact of pore-engineering on their graphitic structure. Figure 3e shows all carbon materials have two major peaks. The peak at  $1587\text{ cm}^{-1}$  (G-band) is originated from the  $sp^2$ -hybridized carbon atoms in the graphite lattice while the peak at  $1329\text{ cm}^{-1}$  (D-band) can be assigned to the defect-induced phonon scatterings. Hence, the intensity ratio between the D- and G-band peaks (D/G ratio) can be utilized to compare the crystallinity of the carbon materials.<sup>[16]</sup> The calculated D/G ratio is listed in Table 1 for comparison. The results show that the addition of the  $\text{SiO}_2$  template has a minor impact. WC-0-0.8 has a D/G ratio of 1.01, which is similar to that of WC-0-0 at 1.00 without adding any templates. WC-3-0 has an increased D/G ratio of 1.03. Considering the elemental analysis results show that heteroatom abundances are similar in WC-3-0 and WC-0-0, the higher D/G ratio of WC-3-0 can be attributed to defects introduced by micropores. Figure 3f shows that the changes in SSA and pore volumes exhibit a good agreement with the changes in Raman D/G ratios, further confirming the capability of the dual template method in tuning the structures of whey powder derived carbon materials.

Besides the pore structures, the concentration of N and S dopants and their configurations can also strongly influence the ORR catalytic activity of carbon electrocatalysts.<sup>[17]</sup> While EDX elemental analysis results show that the pore-engineering does not change the abundances of N and S significantly, we further probed their detailed configurations by high-resolution N1s and S2p X-ray photoelectron spectroscopy (XPS). **Figure 4a** shows that the N1s spectra of the carbon materials can be deconvoluted into four different peaks at 398.4, 400.5, 401.5, and 403.7 eV, which can be assigned to pyridinic-, pyrrolic-, graphitic-, and oxidized-N species, respectively (as illustrated in Figure 4c).<sup>[18]</sup> Further, the S2p spectra in Figure 4b can be split into two peaks. The peaks at 163.9 and 165.2 eV can be assigned to  $S2p_{3/2}$  and  $S2p_{1/2}$  of S-C bonds (as illustrated in Figure 4c).<sup>[19]</sup> The broad peak at a higher binding energy of 168.4 eV can be attributed to oxidized S-O bonds. The relative abundances of N and S in different configurations are listed in Table S1 in SI for comparison.

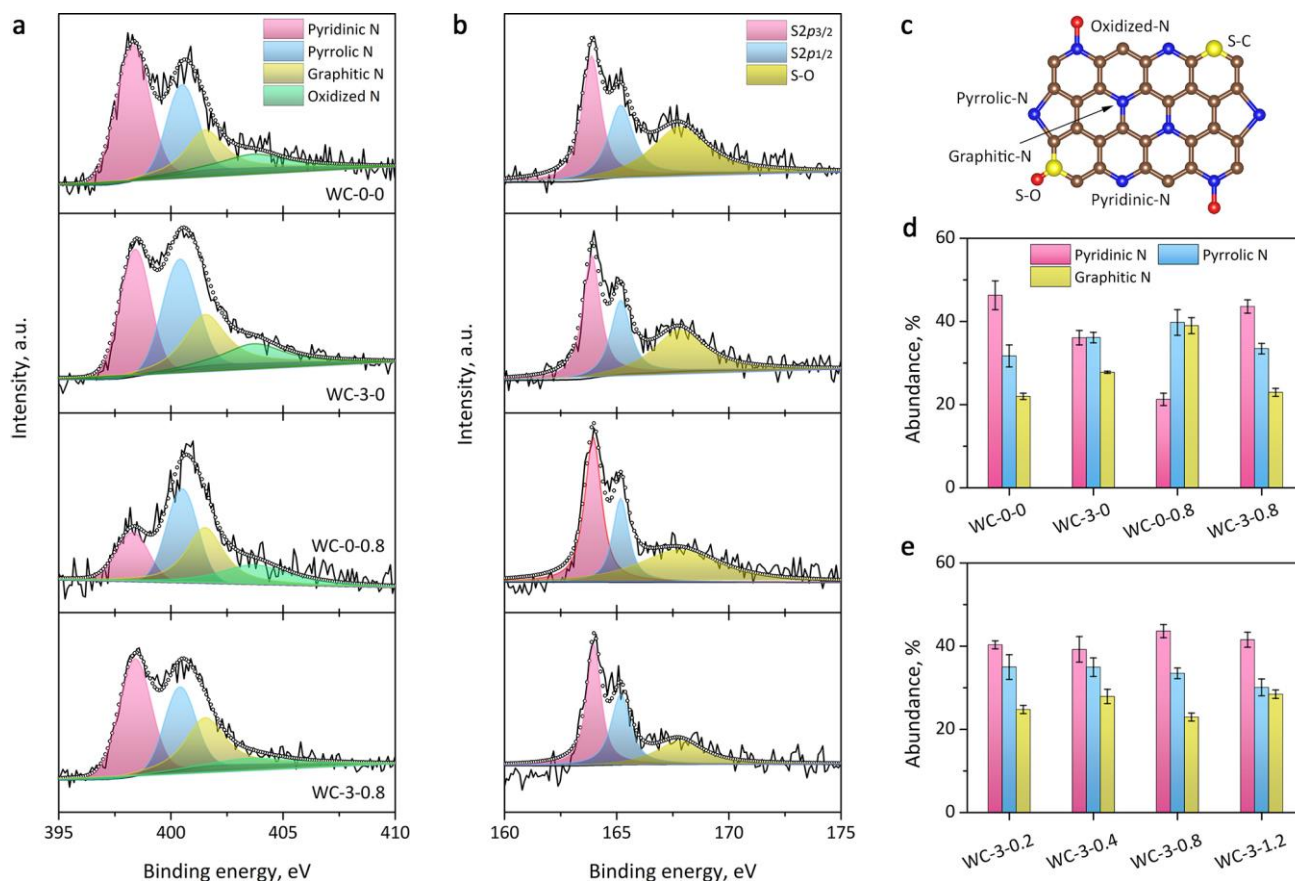


**Figure 4.** High-resolution XPS spectra of (a) N1s and (b) S2p of carbon materials. (c) Schematic illustration of N and S atoms in different configurations. The abundances of N atoms in various configurations in carbon materials with (d) different templates and (e) changing the mass ratios of the SiO<sub>2</sub> template.

Figure 4d shows that WC-0-0 without using any template has the highest abundance of pyridinic N. ZnCl<sub>2</sub> and SiO<sub>2</sub> templates can convert some pyridinic-N into pyrrolic-N. For example, SiO<sub>2</sub> templated WC-0-0.8 has a high abundance of pyrrolic-N (~39.7 %). The pyridinic-N content in the dual-templated WC-3-0.8 was found to be higher over that in WC-0-0.8 and WC-3-0. Besides, more S in the S-C configuration was also found in the dual-templated WC-3-0.8 (68.3 %, Table S1 in SI).

We further explored potential correlations between the mass loading of SiO<sub>2</sub> particles and the configuration of N- and S-dopants. WC-3-y samples (y = 0.2, 0.4, 0.8 and 1.2) shown in Figure S4 in SI were deconvoluted. The abundances of N in different configurations are displayed in Figure 4e.

While the abundances pyridinic- and pyrrolic-N remain largely unchanged, the abundance of graphitic-N drops slightly from WC-3-0.2 to WC-3-0.8, and then increases in WC-3-1.2. This trend is inverse to the trend of the SSA shown in Figure 3f. Initially, more SiO<sub>2</sub> particles generate more pores, which have more edges to accommodate pyridinic- and pyrrolic-N species. Thus, WC-3-0.8 has the highest SSA of 1944.7 m<sup>2</sup> g<sup>-1</sup> and the lowest abundance of graphitic-N at 22.9 %. However, further increasing the mass loading of SiO<sub>2</sub> reduces the SSA to 1475.7 m<sup>2</sup> g<sup>-1</sup> in WC-3-1.2, and its abundance of graphitic-N rises to 28.4 %. In contrast, Table S1 in SI shows that the abundance of S-C has minor changes, suggesting that the configuration of S is not affected by the mass loading of SiO<sub>2</sub> particles.

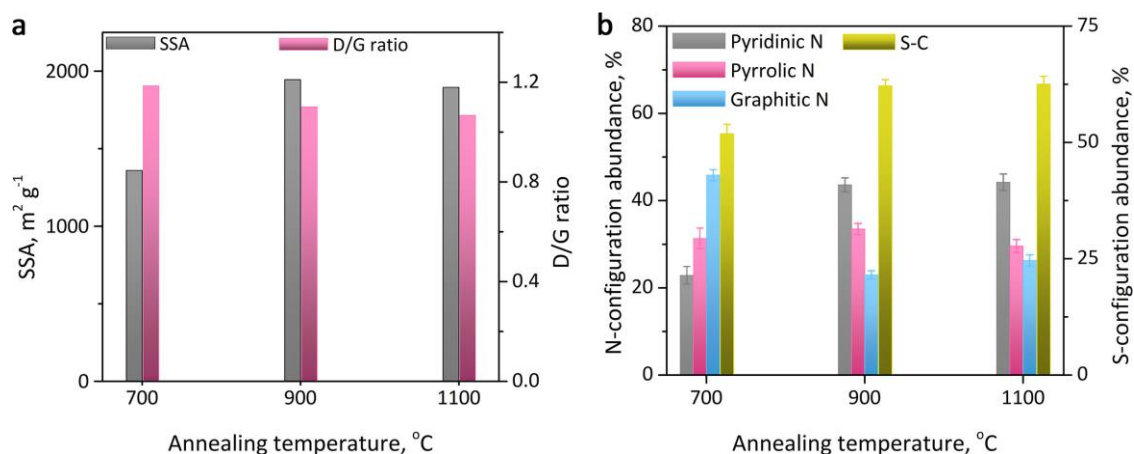


**Figure 5.** Impact of carbonization temperatures on (a) SSA and Raman D/G ratio and (b) N and S configurations of whey powder derived carbon materials.

The impact of carbonization temperature on the pore structure and heteroatom dopant configurations was also investigated. Two additional WC-3-0.8 samples were prepared by carbonization at 700 and 1100 °C (denoted as WC-3-0.8-700 and WC-3-0.8-1100, respectively). First, SEM images in Figure S5 in SI show that the two samples have minor morphology changes compared to WC-3-0.8-900. Their adsorption isotherms in Figure S6 in SI shows that WC-3-0.8-700 has a reduced SSA and pore volume, while the parameters of WC-3-0.8-1100 are similar to those of WC-3-0.8-900, as summarized in Table 1 and **Figure 5a**. The pore size distributions of the three samples are also similar except that WC-3-

0.8-700 has a slightly lower micropore volume, which may be due to the fact that the carbonization at 700 °C is not high enough to remove Zn efficiently. Overall, when the carbonization temperature is above 900 °C, the pore structure of whey powder derived carbon materials has minor changes. Next, EDX elemental analysis of N, S, and O listed in Table 1 show that abundances of heteroatoms decrease with the increase of carbonization temperature. Further, Raman spectra in Figure S7 and the corresponding D/G ratios shown in Figure 5a indicate that the defect density is lower at higher carbonization temperatures. Last, Figure S8 in SI shows N1s and S2p XPS spectra of the three samples. The abundances of N and S in different configurations are shown in Figure 5b. The abundance of S atoms in the S-C configuration is higher at 900 and 1100 °C. N atoms also exhibit substantial changes. The abundance of pyridinic N is higher at 900 and 1100 °C, while the abundance of pyrrolic N has minor variations at the three temperatures, while the abundance of graphitic N also has small changes above 900 °C. Since the total N abundance in WC-3-0.8-1100 is only 1.9 at.%, which is much lower than that in WC-3-0.8-900 at 4.6 at.%. Thus, WC-3-0.8-900 contains more pyridinic N, which is beneficial for enhancing the catalytic activity for ORR.<sup>[5b]</sup>

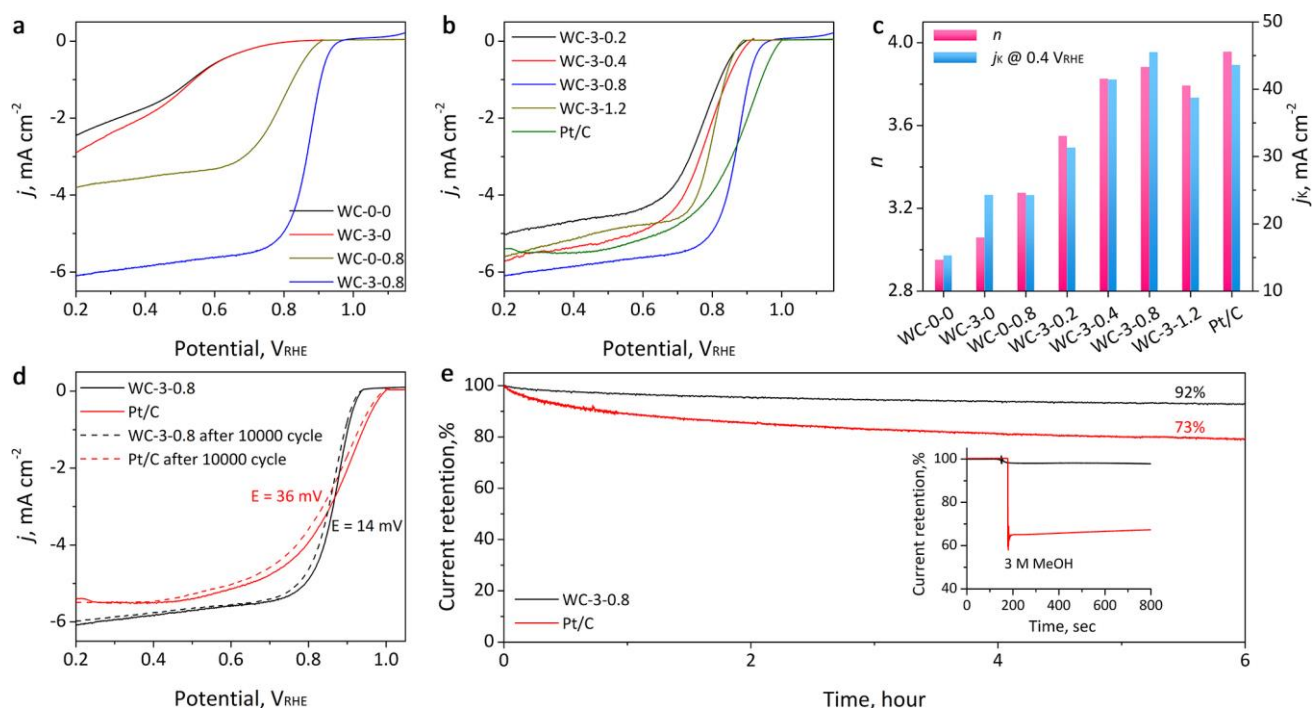


**Figure 6.** Electrochemical performance of carbon electrocatalysts tested in 0.1 M KOH electrolyte. (a) ORR LSV curves of carbon electrocatalysts obtained by (a) using different types of templates and (b) different mass loadings of SiO<sub>2</sub> template. (c) Comparison of ORR kinetic parameters at 0.4 V<sub>RHE</sub>. (d) Durability tests by (d) CV cycling and (e) chronopotentiometry methods. The inset in (e) displays the MeOH tolerance test result.

The whey powder derived carbon materials were used as electrocatalysts for ORR. Their ORR catalytic activity was tested in O<sub>2</sub> saturated 0.1 M KOH electrolyte. **Figure 6a** compares the LSV curves of the carbon electrocatalysts synthesized using different templates. The dual templated WC-3-0.8 exhibits superior performance with the largest onset potential of 0.98 V vs. V<sub>RHE</sub> and the highest limiting current density of 6.08 mA cm<sup>-2</sup> at 0.2 V. The single templated samples (WC-3-0 and WC-0-0.8) show inferior performances with more negative onset potentials and lower limiting current densities. It is noteworthy that even though WC-3-0 has the SSA 10 times higher than the non-porous WC-0-0, WC-3-0 only exhibits a minor improvement in its ORR activity compared to WC-0-0. And WC-3-0 is outperformed by WC-0-0.8 with only 1/3 of its SSA but containing more mesopores. These observations suggest that mass transfer resistances of electrolyte ions and reaction intermediates in micropores is a critical limiting factor for the ORR catalytic activity of porous carbon electrocatalysts derived from whey powders.

**Table 2.** ORR performance parameters of carbon electrocatalysts derived from whey powders.

Sample	ORR activity		
	E <sub>1/2</sub> , V	n <sup>[a]</sup>	j <sub>K</sub> , mA cm <sup>-2</sup> [a]
WC-3-0.2	0.764	3.55	31.22
WC-3-0.4	0.783	3.79	38.64
<b>WC-3-0.8</b>	<b>0.875</b>	<b>3.88</b>	<b>45.40</b>
WC-3-1.2	0.801	3.83	41.33
WC-3-0	0.515	3.06	23.18
WC-0-0.8	0.789	3.28	30.17
WC-0-0	0.521	2.95	15.19
Pt/C	0.887	3.96	43.50

[a] calculated by K-L plots at 0.4 V<sub>RHE</sub>.

We further studied how the pore-engineering influences the ORR catalytic activity of the dual-templated carbon electrocatalysts. Figure 6b shows that WC-3-0.8 exhibits the highest ORR catalytic activity among all carbon electrocatalysts. When compared to the activity of the commercial 20 wt% Pt/C catalyst, WC-3-0.8 can reach the half-wave potential ( $E_{1/2}$ ) at 0.875 V vs.  $V_{\text{RHE}}$ , which is similar to that of Pt/C at 0.887 V. Further, WC-3-0.8 delivers a limiting current density 16% higher than that of Pt/C. K-L plots of WC-3-0.8 are shown in Figure S9, and they were used to calculate the electron transfer number ( $n$ ) and kinetic limiting current density ( $j_k$ ). The results are listed in Table 2 and compared in Figure 6c. WC-3-0.8 has the largest  $n$  of 3.88 and  $j_k$  of 45.40 mA cm<sup>-2</sup> among all carbon electrocatalysts, which is also comparable to those of Pt/C at 3.96 and 43.50 mA cm<sup>-2</sup>, respectively. Figure 6c shows that the changes in the catalytic activities of carbon electrocatalysts exhibit a similar trend as those in their structure properties, including SSA and pore volume. We also compared the catalytic activity of WC-3-0.8 obtained at different carbonization temperatures, and the results are shown in Figure S10 in SI. WC-3-0.8-900 shows higher activity than WC-3-0.8-700 and WC-3-0.8-1100. Besides, the performance of WC-3-0.8 one of the best among recently reported biomass-derived carbon electrocatalysts (see a detailed comparison in Table S2 in SI).

The durability of WC-3-0.8 was also assessed. As shown in Figure 6d, the LSV curve of WC-3-0.8 exhibits a shift of ~14 mV after 10000 cyclic voltammetry (CV) cycles scanned between 1 to 0 V, which is much smaller than that of Pt/C at 36 mV. Besides, Figure 6e shows that in the durability test carried out by the chronopotentiometric method, WC-3-0.8 can retain ~92% of its initial current intensity after 6 under 0.4 V, which is higher than that of Pt/C at 73%. Moreover, WC-3-0.8 also exhibits much better tolerance toward methanol crossover than Pt/C, as shown in the inset of Figure 6e. The surface morphology of WC-3-0.8 has negligible alternations after the stability test (Figure S11 in SI).

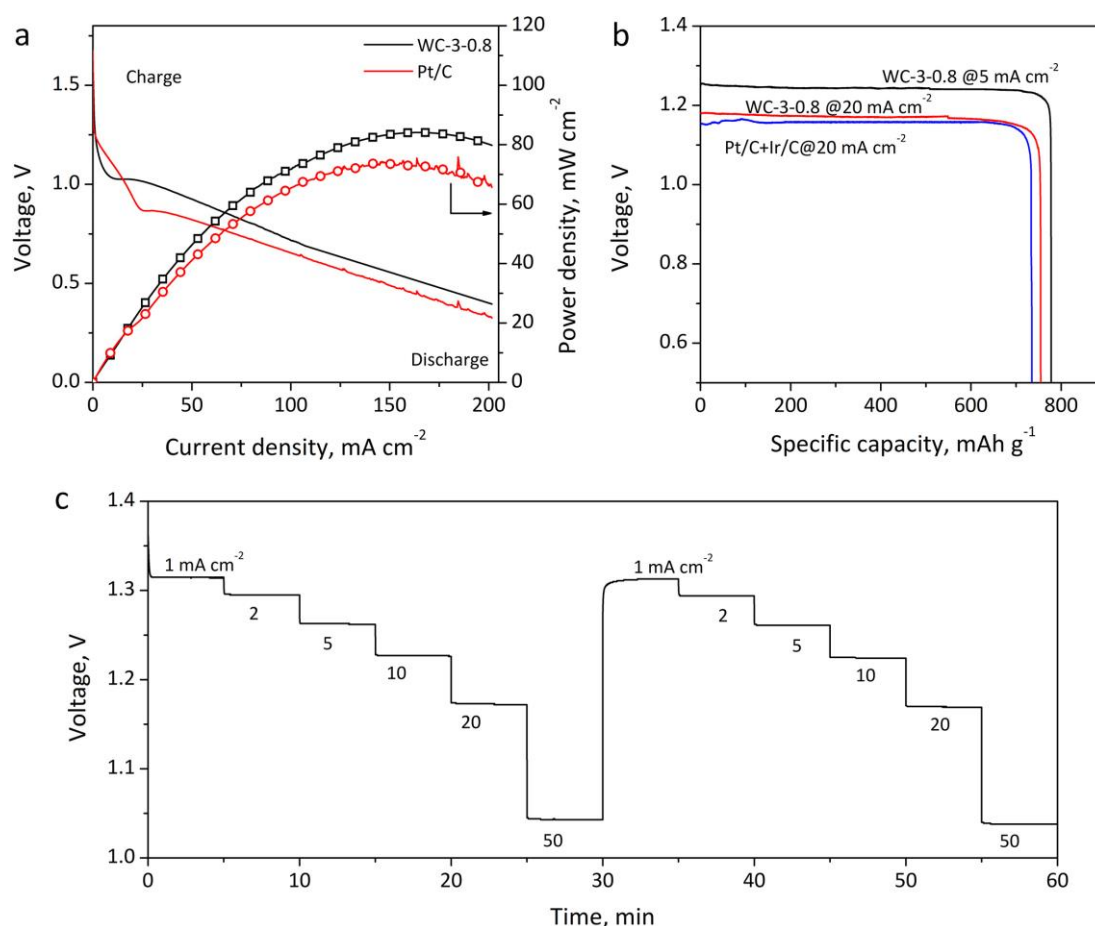


**Figure 7.** The performance of primary ZABs assembled using WC-3-0.8 as ORR electrocatalyst. (a) Galvanodynamic discharge curves and power density and (b) the galvanostatic specific capacity of ZABs fabricated using WC-3-0.8 and Pt/C. (c) Galvanostatic discharge curves of the ZAB-WC-3-0.8 collected at different current densities.

Since WC-3-0.8 has excellent ORR catalytic activity, we further demonstrated their practical applications as ORR catalysts in primary ZABs. A ZAB was assembled using a gas-diffusion electrode deposited with WC-3-0.8 with a mass loading of 0.5 mg cm<sup>-2</sup> (denoted as ZAB-WC-3-0.8). A Zn foil was used as a metal electrode, and a mixture of 6 M KOH with 0.5 M Zn(CH<sub>3</sub>CO<sub>2</sub>)<sub>2</sub> was used as the electrolyte. Another ZAB was assembled as a reference by replacing WC-3-0.8 with Pt/C at the same mass loading (denoted as ZAB-Pt/C). The battery performances were tested in ambient conditions at 25 °C. As shown in the galvanodynamic charge-discharge curves in Figure 7a, ZAB-WC-3-0.8 delivers an open circuit potential of 1.43 V, which is similar to 1.45 V of ZAB-Pt/C. ZAB-WC-3-0.8

outperforms ZAB-Pt/C when the discharge current density is higher than  $\sim 20 \text{ mA cm}^{-2}$ . The maximum power density of ZAB-WC-3-0.8 at  $84.1 \text{ mW cm}^{-2}$  is  $\sim 10\%$  higher than that of ZAB-Pt/C at  $73.5 \text{ mW cm}^{-2}$ . Further, the specific capacity of ZAB-WC-3-0.8 reaches  $779.5$  and  $746.2 \text{ mAh g}^{-1}$  at the discharge current density of  $5$  and  $20 \text{ mA cm}^{-2}$ , respectively, which are higher than the  $735.1 \text{ mAh g}^{-1}$  of ZAB-Pt/C. ZAB-WC-3-0.8 also exhibits robust responses when the discharge current density changes. As shown in Figure 6c, the voltage of ZAB-WC-3-0.8 can quickly stabilize when the current density increases from  $1$  to  $50 \text{ mA cm}^{-2}$ . Its output voltage returns to its original value when the current density is set back to  $1 \text{ mA cm}^{-2}$ , indicating excellent performance with fast responses.

## Conclusion

In summary, using  $\text{ZnCl}_2$  and fumed  $\text{SiO}_2$  as templates, the dual-template method can effectively tune pore structures of carbon materials derived from whey powders.  $\text{ZnCl}_2$  created abundant micropores and small mesopores, while  $\text{SiO}_2$  particles produced large interconnected mesopores. The hierarchical pores provide a large surface area accessible to electrolyte ions and reaction intermediates. The optimal carbon material (WC-3-0.8) can deliver the highest SSA of  $1944.7 \text{ m}^2 \text{ g}^{-1}$  and superior ORR activity with  $E_{1/2}$  at  $0.875 \text{ V}$ ,  $n$  of  $3.88$ , and  $j_K$  of  $45.40 \text{ mA cm}^{-2}$ , comparable to the commercial Pt/C catalyst. The ZAB assembled using WC-3-0.8 has an open circuit potential of  $1.43 \text{ V}$ , the maximum power density of  $84.1 \text{ mW cm}^{-2}$ , the specific capacity of  $779.5 \text{ mAh g}^{-1}$  at the discharge current density of  $5 \text{ mA cm}^{-2}$ , which outperform the ZAB fabricated using commercial Pt/C catalyst. This work opens up the opportunity to transform abundant biomaterials into high-value-added electrocatalysts for energy storage and conversion applications.

## Experimental section

*Material synthesis.* Whey powder (NKD Whey Protein Isolate) was obtained from NKD Co., which contains  $83.3 \text{ wt.}\%$  protein,  $10 \text{ wt.}\%$  carbohydrate, and  $6.7 \text{ wt}\%$  fat. Whey powder derived carbon

materials were synthesized using the same procedure while the type and amount of template materials were varied. Typically, 1 g of the whey powders were dissolved in 20 mL acetone under stirring. Different quantities of  $\text{ZnCl}_2$  (99.9%, Sigma) and fumed  $\text{SiO}_2$  (specific surface area of  $200 \text{ m}^2 \text{ g}^{-1}$ , Sigma) were added to the acetone solution. The mixture was further stirred for 2 h before it was heated and dried under stirring to remove all solvent. The solid material was grounded into fine powders, put in an alumina boat, and placed in the middle of a tube furnace (BTC-1200, BEQ, tube diameter = 50 mm). The furnace was flushed with Ar (99.999%, BOC) for 30 min before the sample was heated to  $900 \text{ }^\circ\text{C}$  under Ar flow (200 sccm) at a ramp rate of  $5 \text{ }^\circ\text{C min}^{-1}$ . The solid material was held at  $900 \text{ }^\circ\text{C}$  for 2 h before cooled down to room temperature under Ar protection. The carbonized material was first refluxed in 3 M KOH to remove  $\text{SiO}_2$ . Next, it was washed by 3 M HCl and a large amount of deionized water to remove Zn residuals. The resulting carbon materials were denoted as WC- $x$ - $y$  (see Table 1), where  $x$  and  $y$  refer to the mass ratios of  $\text{ZnCl}_2$  and  $\text{SiO}_2$  to whey powders, respectively. Two additional carbon materials were synthesized by changing the carbonization temperature to 700 and  $1100 \text{ }^\circ\text{C}$  (denoted as WC-3-0.8-700 and WC-3-0.8-1100, respectively). All carbon materials were dried in an oven at  $80 \text{ }^\circ\text{C}$  for 12 h before electrochemical catalytic activity tests.

*Material characterization.* Surface morphology and elemental composition were characterized by an SEM (Ultra-Plus, Zeiss) equipped with an EDX spectrometer. TEM and STEM-EDX characterization were performed on an electron microscope (JEM-2100, Joel).  $\text{N}_2$  physisorption isotherms were obtained on a surface analyzer (Autosorb-1, QuantaChrome). The SSA was calculated by the BET method, and the pore size distribution was determined by the NL-DFT method. Raman spectra were collected under 532 nm laser irradiation by a Raman microscope (inVia, Renishaw). The chemical composition and configuring of different elements were determined by XPS (K-Alpha+, Thermo Fisher Scientific) with an Al- $\text{K}\alpha$  source (1486.3 eV).

*Electrode preparation.* Carbon materials were first ground into fine powders. About 5 mg of the ground carbon powder was added in a water/isopropanol alcohol (IPA) solution (1:9 v/v) with 0.05

wt. % Nafion 117 (Sigma) at a concentration of 5 mg mL<sup>-1</sup>. The solution was then homogenized by an ultrasonic bath for 1 h and served as catalyst ink to prepare electrodes. Working electrodes were prepared by drop-casting 20 μL of catalyst ink on pre-polished glassy carbon rotating disk electrodes (RDEs) (5 mm in diameter, Pine Research). The areal mass loading is about 0.5 mg cm<sup>-2</sup>. The RDEs were dried at the ambient condition overnight. The commercial Pt/C (20 wt.% Pt on Vulcan XC-72 carbon black, Sigma) was used as a reference catalyst for ORR. They were cast on electrodes using the same method. At least three electrodes were prepared and tested for every catalyst sample to ensure result reproducibility.

*Electrochemical performance test.* The activity for ORR was evaluated using the three-electrode configuration. A saturated calomel electrode and a Pt mesh were used as the reference and counter electrode, respectively. All potentials were calibrated to a reversible hydrogen electrode (RHE). Electrocatalytic tests were performed on an electrochemical workstation (660E, CHI Instrument) in 0.1 M KOH electrolyte. The electrolyte was saturated with either Ar or O<sub>2</sub> for 30 min before performance measurements. Cyclic voltammetry (CV) curves were recorded at 50 mV s<sup>-1</sup>. Linear sweep voltammetry (LSV) curves were collected from 400 to 2500 rpm at 5 mV s<sup>-1</sup> without *iR* compensation. Electron transfer number (*n*) and the kinetic limiting current density (*j<sub>k</sub>*) of different catalysts were calculated by the Koutechky-Levich (K-L) equation, as shown below:

$$1/j = 1/j_L + 1/j_K = 1/B\omega^{1/2} + 1/j_K \quad (1)$$

$$B = 0.62nFC_0(D_0)^{2/3}\nu^{-1/6} \quad (2)$$

$$j_K = nFkC_0 \quad (3)$$

where *j* is the measured current density, *j<sub>k</sub>* and *j<sub>L</sub>* are the kinetic- and diffusion- limiting current densities,  $\omega$  is the angular velocity, *n* is electron transfer number, *F* is the Faraday constant, *C<sub>0</sub>* is the saturated concentration of O<sub>2</sub> in 1 M KOH at room temperature, *D<sub>0</sub>* is diffusion coefficient of oxygen in water,  $\nu$  is the kinematic viscosity of the electrolyte, and *k* is the electron-transfer rate constant.

*Zn-air battery assembly and tests.* Gas diffusion electrodes were prepared by drop-casting the catalyst ink on a piece of carbon cloth (2×2 cm<sup>2</sup> in size) with a mass loading of 0.5 mg cm<sup>-2</sup>. A Zn foil was used as the metal electrode, and a mixture of 6 M KOH with 0.2 M ZnCl<sub>2</sub> aqueous solution was used as the electrolyte. Zn-air batteries were assembled by sandwiching the gas diffusion electrode, the Zn-metal electrode, and the electrolyte together. Several reference batteries were also assembled by using gas diffusion electrodes prepared by the reference Pt/C catalyst with the same areal loading. The battery performance was tested on a battery test station (Land).

### Acknowledgment

The Australian Research Council supported this work under the Future Fellowships scheme (FT160100107) and Discovery Programme (DP180102210), and we acknowledge technical assistance provided by the Sydney Microscopy & Microanalysis, a Core Research Facility of the University of Sydney.

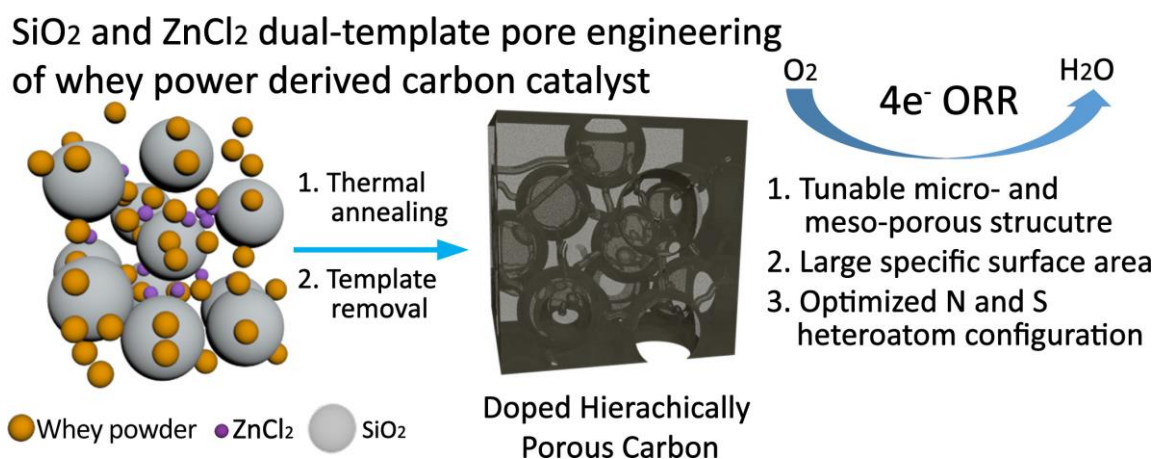
### References

- [1] a) G. Wu, A. Santandreu, W. Kellogg, S. Gupta, O. Ogoke, H. Zhang, H.-L. Wang and L. Dai, *Nano Energy* **2016**, *29*, 83-110; b) P. Gu, M. Zheng, Q. Zhao, X. Xiao, H. Xue and H. Pang, *J. Mater. Chem. A* **2017**, *5*, 7651-7666; c) X. Li, F. Dong, N. Xu, T. Zhang, K. Li and J. Qiao, *ACS Appl. Mater. Interfaces* **2018**, *10*, 15591-15601; d) B. C. H. Steele and A. Heinzl, *Nature* **2001**, *414*, 345-352.
- [2] a) Y. Nie, L. Li and Z. Wei, *Chem. Soc. Rev.* **2015**, *44*, 2168-2201; b) S. Sui, X. Wang, X. Zhou, Y. Su, S. Riffat and C.-j. Liu, *J. Mater. Chem. A* **2017**, *5*, 1808-1825; c) M. Liu, Z. Zhao, X. Duan and Y. Huang, *Adv. Mater.* **2019**, *31*, 1802234.
- [3] a) X. Liu and L. Dai, *Nat. Rev. Mater.* **2016**, *1*, 1-12; b) H. F. Wang, C. Tang and Q. Zhang, *Adv. Funct. Mater.* **2018**, *28*, 1803329; c) D. Liu, L. Dai, X. Lin, J. F. Chen, J. Zhang, X. Feng, K. Müllen, X. Zhu and S. Dai, *Adv. Mater.* **2019**, *31*, 1804863.

- [4] a) K. Gong, F. Du, Z. Xia, M. Durstock and L. Dai, *Science* **2009**, 323, 760; b) C. Hu and L. Dai, *Angew. Chem. Int. Ed.* **2016**, 55, 11736-11758; c) L. Yang, J. Shui, L. Du, Y. Shao, J. Liu, L. Dai and Z. Hu, *Adv. Mater.* **2019**, 31, 1804799; d) C. Hu, Y. Xiao, Y. Zou and L. Dai, *Electrochem. Energy Rev.* **2018**, 1, 84-112; e) S. Zhao, D. W. Wang, R. Amal and L. Dai, *Adv. Mater.* **2019**, 31, 1801526.
- [5] a) J. Zhang, L. Qu, G. Shi, J. Liu, J. Chen and L. Dai, *Angew. Chem. Int. Ed.* **2016**, 55, 2230-2234; b) H. B. Yang, J. Miao, S.-F. Hung, J. Chen, H. B. Tao, X. Wang, L. Zhang, R. Chen, J. Gao and H. M. Chen, *Sci. Adv.* **2016**, 2, e1501122; c) Q. Lv, W. Si, J. He, L. Sun, C. Zhang, N. Wang, Z. Yang, X. Li, X. Wang and W. Deng, *Nat. Commun.* **2018**, 9, 1-11.
- [6] a) G. A. Ferrero, K. Preuss, A. B. Fuertes, M. Sevilla and M. M. Titirici, *J. Mater. Chem. A* **2016**, 4, 2581-2589; b) H. Yan, *Chem. Commun.* **2012**, 48, 3430-3432.
- [7] L. Zhang, X. Yang, F. Zhang, G. Long, T. Zhang, K. Leng, Y. Zhang, Y. Huang, Y. Ma, M. Zhang and Y. Chen, *J. Am. Chem. Soc.* **2013**, 135, 5921-5929.
- [8] a) C. Long, L. Jiang, X. Wu, Y. Jiang, D. Yang, C. Wang, T. Wei and Z. Fan, *Carbon* **2015**, 93, 412-420; b) J. Wang and S. Kaskel, *J. Mater. Chem.* **2012**, 22, 23710-23725; c) Y. Li, H. Zhang, Y. Wang, P. Liu, H. Yang, X. Yao, D. Wang, Z. Tang and H. Zhao, *Energy Environ. Sci.* **2014**, 7, 3720-3726; d) L. Wei, H. E. Karahan, K. Goh, W. Jiang, D. Yu, Ö. Birer, R. Jiang and Y. Chen, *J. Mater. Chem. A* **2015**, 3, 7210-7214; e) J. Pampel and T. P. Feller, *Adv. Energy Mater.* **2016**, 6, 1502389.
- [9] J. Deng, M. Li and Y. Wang, *Green Chem.* **2016**, 18, 4824-4854.
- [10] a) M. Borghei, J. Lehtonen, L. Liu and O. J. Rojas, *Adv. Mater.* **2018**, 30, 1703691; b) L. Wei, H. E. Karahan, S. Zhai, Y. Yuan, Q. Qian, K. Goh, A. K. Ng and Y. Chen, *J. Energy Chem.* **2016**, 25, 191-198.
- [11] G. Chegini; and M. Taheri, *Middle-East J. Sci. Res.* **2013**, 13, 1377-1387.
- [12] J. G. Zadow in *Whey and Whey Powders / Production and Uses*, (Ed. B. Caballero), Academic Press, Oxford, **2003**, pp. 6147-6152.
- [13] C. Saka, *J. Anal. Appl. Pyrol.* **2012**, 95, 21-24.

- [14] a) J. Park, Y. Nabaee, T. Hayakawa and M. A. Kakimoto, *ACS Catal.* **2014**, *4*, 3749-3754; b) X. R. Wen, D. S. Zhang, L. Y. Shi, T. T. Yan, H. Wang and J. P. Zhang, *J. Mater. Chem.* **2012**, *22*, 23835-23844; c) T. Liu, L. Y. Zhang, W. You and J. G. Yu, *Small* **2018**, *14*.
- [15] a) Y. Ren, Z. Ma, R. E. Morris, Z. Liu, F. Jiao, S. Dai and P. G. Bruce, *Nat. Commun.* **2013**, *4*, 2015-2015; b) J. Shen, A. Liu, Y. Tu, G. Foo, C. Yeo, M. B. Chan-Park, R. Jiang and Y. Chen, *Energy Environ. Sci.* **2011**.
- [16] F. Tuinstra and J. L. Koenig, *J. Chem. Phys.* **1970**, *53*, 1126-1130.
- [17] C. V. Rao, C. R. Cabrera and Y. Ishikawa, *J. Phys. Chem. Lett.* **2010**, *1*, 2622-2627.
- [18] L. Ma, J. Liu, S. Lv, Q. Zhou, X. Shen, S. Mo and H. Tong, *J. Mater. Chem. A* **2019**, *7*, 7591-7603.
- [19] J. P. Paraknowitsch, A. Thomas and J. Schmidt, *Chem. Commun.* **2011**, *47*, 8283-8285.

### Graphitic abstract



Pore structures of whey powder derived carbon materials are engineered by using ZnCl<sub>2</sub> and SiO<sub>2</sub> particles as dual templates. A large surface area of 1944 m<sup>2</sup> g<sup>-1</sup> is obtained at an optimal mass ratio of whey powder: ZnCl<sub>2</sub>: SiO<sub>2</sub> = 1: 3: 0.8, which delivers excellent catalytic activity for the oxygen reduction reaction.